AIAA-97-1595

Aeroacoustic Measurements of a Wing-Flap Configuration

Kristine R. Meadows
Thomas F. Brooks
William M. Humphreys
William H. Hunter
Carl H. Gerhold

NASA Langley Research Center
Hampton, VA

3rd AIAA/CEAS Aeroacoustics Conference
May 12-14, 1997 / Atlanta, GA

AEROACOUSTIC MEASUREMENTS OF A WING-FLAP CONFIGURATION

Kristine R. Meadows *
Thomas F. Brooks †
William M. Humphreys ‡
William W. Hunter §
Carl H. Gerhold ¶
Fluid Mechanics and Acoustics Division
NASA Langley Research Center
Hampton, VA 23681-0001

Abstract

Aeroacoustic measurements are being conducted to investigate the mechanisms of sound generation in high-lift wing configurations, and initial results are presented. The model is approximately 6 percent of a full scale configuration, and consists of a main element NACA $63_2 - 215$ wing section and a 30 percent chord half-span flap. Flow speeds up to Mach 0.17 are tested at Reynolds number up to approximately 1.7 million. Results are presented for a main element at a 16 degree angle of attack, and flap deflection angles of 29 and 39 degrees. The measurement systems developed for this test include two directional arrays used to localize and characterize the noise sources, and an array of unsteady surface pressure transducers used to characterize wave number spectra and correlate with acoustic measurements. Sound source localization maps show that locally dominant noise sources exist on the flap-side edge. The spectral distribution of the noise sources along the flap-side edge shows a decrease in frequency of the locally dominant noise source with increasing distance downstream of the flap leading edge. Spectra are presented which show general spectral characteristics of Strouhal dependent flow-surface interaction noise. However, the appearance of multiple broadband tonal features at high frequency indicates the presence of aeroacoustic phenomenon following different scaling characteristics. The scaling of the high frequency aeroacoustic phenomenon is found to be different for the two flap deflection angles tested. Unsteady surface pressure measurements in the vicinity of the flap edge show high coherence levels between adjacent sensors on the flap-side edge and on the flap edge upper surface in a region which corresponds closely to where the flap-side edge vortex begins to spill over to the flap upper surface. The frequency ranges where these high levels of coherence occur on the flap surface are consistent with the frequency ranges in which dominant features appear in far field acoustic spectra. The consistency of strongly correlated unsteady surface pressures and far field pressure fluctuations suggests the importance of regions on the flap edge in generating sound.

Introduction

With the advent of increasingly strict noise regulations and quieter aircraft engines, there is renewed interest in the abatement of airframe noise. Airframe noise is the unwanted sound generated by the nonpropulsive elements of the aircraft, and results from air flow over the fuselage, and items such as the wings, high-lift devices, landing gear, and wheel wells. Airframe noise is most noticeable when the aircraft is approaching the airport and landing, because the engines are at low power, the high-lift systems are deployed, and the undercarriage is down.

Although airframe noise has been studied extensively since the 1970's [1], there is still limited understanding of the physical mechanisms which are responsible for generating airframe noise. Of particular recent interest is the sound generated by multi-

*Research Scientist, Aerodynamic and Acoustics Methods Branch, Member AIAA.
†Senior Research Scientist, Aeroacoustics Branch, Associate Fellow AIAA.
‡Research Scientist, Measurement Sciences and Technology Branch, Member AIAA.
§Senior Research Scientist, Measurement Sciences and Technology Branch.
¶Senior Research Scientist, Aeroacoustics Branch, Member AIAA.

element airfoils used in high-lift systems installed on most commercial aircraft. Several experimental studies have contributed towards better understanding of sound due to these high-lift devices. In noise studies of a wing configuration consisting of a main airfoil element and a flap in the wake of landing gear, Block [2] noted that flaps contribute significantly to the airframe noise. Later Kendall [3] and Kendall and Ahtye [4] used an elliptical acoustic mirror to produce sound source localization maps, and showed that significant sound sources exist at the gap between the main element and flap and at the flap-side edge. Fink and Schlinker [5] reinforced this finding and published the spectral characteristics of these sources. Miller et al. [6] and McInerny et al. [7] took simultaneous acoustic and surface pressure measurements to characterize the correlations between the near- and far- field unsteady pressures on a single airfoil and on an airfoil-flap configuration, respectively. Miller et al. [6] found the flap-side edge to be a significant sound source, and noted that the directivity of the sound sources was modified by wing diffraction. Cross-correlation analysis performed by McInerny et al. [7] showed that well-ordered turbulent structures on the airfoil tip radiated to the far field as sound. A recent series of experiments by Storms, et al. [8] focused on the flowfield in the vicinity of a generic flap and reported the presence of a dual vortex system. Khorrami et al. [9] conducted numerical experiments which showed excellent agreement with the major features observed in the experiment of Storms, et al. [8].

Several models have been developed for sound generation by wing edges. The rotorcraft community has developed empirical models for the sound generated by the tip of the rotor blade. George, et al. [10] used trailing edge noise theory to develop an empirical model of the 'tip noise' mechanism. George and Chou [11] updated the original model by including more pertinent tip vortex data and modifying length and velocity scales. Brooks and Marcolini [12] employed near wake velocity and noise measurements to quantify and validate the George and Chow model. The model was shown to be useful for rotor noise prediction [13, 14]. Theoreticians have developed models specifically to describe the flap edge phenomena. Hardin [15] developed a two dimensional model which considers the chordwise boundary layer vorticity being swept around the edge by the spanwise flow on the flap. Hardin's model predicted that flap edge noise could be more intense than trailing edge noise, in agreement with experimental observations. Sen [16, 17] recently updated Hardin's model to account for finite thickness of the flap edge. Khorrami et al. [9] recently proposed a vortex instability model and a shear layer model to describe sound generation by instabilities in the side edge vortex and the shear layer. The validity of these theoretical models is yet to be determined.

The purpose of this effort is to define and understand the generation and radiation of noise from a basic high-lift wing-flap configuration so that accurate prediction tools can be developed to guide wing design and/or flight procedures for noise reduction. A model consisting of a main element NACA $63_2 - 215$ wing section and a 30 percent chord half-span flap is tested up to flow speeds of Mach 0.17 in an anechoic open jet wind tunnel facility [18]. The model boundary layer is tripped by a 1 inch strip of serrated tape located on the pressure side of the main wing and a 0.25 inch strip on the leading edge of the flap at the stagnation point. The model is approximately 6 percent of full scale, and is tested at Reynolds number based on chord of up to 1.7×10^6. Both far field acoustic and unsteady surface pressure measurements are made. Two complementary directional microphone arrays and are used to identify and characterize noise sources. A large aperture directional array (LADA) is used to define the dominant noise source regions along the flapped wing configuration model. Locally dominant noise source regions are identified by producing high spatial resolution noise source localization maps along the airfoil surface. These noise sources are quantified by the use of a small aperture directional array (SADA). The SADA is constructed with a small diameter and is readily moved about the model. SADA is designed and its data processed for quantitative spectral measurements. An array of unsteady pressure transducers is used to detail the unsteady flow characteristics along the airfoil surface. The surface pressure data are acquired simultaneously with the acoustic array data so that meaningful correlations between the surface aerodynamics and far field sound can be made.

Test Setup

The experiments were conducted in the Quiet Flow Facility (QFF) at the NASA Langley Research Center. The QFF is an open-jet facility designed specifically for anechoic acoustic testing. The test chamber is configured to minimize acoustic reflections, and the flow circuit employs baffles, turbulence screens and turning vanes to ensure low turbulence quiet airflow from the open jet [18]. For the purposes of this experiment, side plates are placed on the short sides of a 2 by 3 foot rectangular nozzle and mounted vertically to hold the airfoil model.

Side plate edges were contoured to reduce edge noise. Acoustic foam was placed on the nozzle body, side plate edges, side plate supports and microphone supports to reduce acoustic reflections from these surfaces.

The model is comprised of a NACA 63_2-215 main airfoil element with a 30 percent chord half-span Fowler flap. The cross-section for the model configurations is shown in Figure 1. The model section is approximately 6 percent of a full-scale configuration. The main element chord is 16 inches; the flap chord is 4.5 inches; the full span is 36 inches. The main element and flap are fully instrumented with static pressure ports and unsteady pressure transducers as shown in Table 1.

Table 1. Instrumentation on Model used in Airframe Noise Testing.

	Main Element	Flap
Unsteady Pressure Sensors		
Kulites (LQ-34-064-5A)	94	79
Endevcos (8507C-2)	2	9
Static Pressure Ports	18	10

Measurement Systems

Large aperture directional array (LADA)

The LADA is used to identify locally dominant noise sources by producing high spatial resolution noise source localization maps along the airfoil surface. To achieve these design goals, 35 1/4 in B&K model 4135 microphones are placed in a two dimensional array pattern consisting of logarithmic spirals. The primary benefit of this array pattern, which was originally conceived by R. Doughtery of Boeing and further developed and implemented by R. Dougherty and J. Underbrink [19], is the elimination of redundancies in the co-array pattern [20]. Elimination of redundancies in the array pattern minimizes the array side lobes and increases the dynamic range.

The array consists of five spirals of seven microphones each with the inner-most microphones lying on a 1-inch radius and the outer-most on a 17-inch radius. The array pattern is shown in Figure 2 with the dots representing the microphone positions. A 48-inch diameter fiber glass panel provides the mounting surface where all 35 microphones are flush mounted. A pan-tilt scan unit is used as a mounting interface between the array and a rigid tripod support. Installation of the array in the QFF is shown in the photograph of Figure 3. In this photograph, the model is visible through the plexiglass in the side plates. The flow comes from the nozzle in the floor of the QFF. The LADA is shown on the pressure side of the model. For the results presented here, alignment of the array is parallel to the model airfoil, set to a 16-degree angle-of-attack. The array center is 48 inches away from and aligned with the mid-span of the airfoil trailing edge. At this position, the spatial resolution of the LADA defined here as the width of the main lobe attenuated 3 dB from the maximum level, is 1.5λ, where λ is the wavelength.

Small Aperture Directional Array (SADA)

The SADA is used to measure the directivity and spectra of selected portions of the wing-flap model. The photograph of Figure 4 shows the SADA mounted on a pivotal boom on the suction side of the model. The pivotal boom is used to position the SADA for directivity measurements. The pivot center is always centered about the trailing edge of the wing main element, although this is not necessary for the array to steer at different areas of the wing-flap model. The face of the array can be placed at a broad range of azimuth and elevation angles, while the SADA distance to the wing-flap center is maintained at 5 feet. Figure 5 is a close-up view of the SADA in calibration mode.

The small size of SADA allows it to be readily moved about the model, but this convenience is not the reason it can be used for directivity measurements. This is made possible by (1) its small aperture compared to the distance from the noise source region of interest and (2) a special microphone sensor geometry and processing methodology to keep the sensing-area's spatial resolution constant over broad frequency ranges. The small aperture (which effectively decreases with frequency as described below) compared to source distance puts all the sensors within narrow portions of the studied noise sources' directivities. For the test conditions presented here, the SADA is positioned at 5 feet away from the model and encompasses about 7 deg of model directivity.

A close-up photo of SADA in a calibration setup is shown in Figure 5, and a sketch of the microphone locations in the array plane is shown in Figure 6. The thirty-three one-eighth inch diameter B&K model 4133 microphones, with one-quarter inch diameter pre-amplifiers, are projected from an acoustically treated frame. There is a center microphone and four rings (irregular circles) of eight microphones each. Each ring is twice the "diameter" of the ring it encloses. For processing reasons as described be-

low, the microphones are subdivided into three subarrays or clusters of 17 microphones each. Cluster c_1 is defined by microphones (mics) 1-17; cluster c_2 by mic 1 and mics 10-25; and cluster c_3 by mic 1 and mics 18-33. The "diameters" of the clusters are $D_1 = 1.94$ in., $D_2 = 3.88$ in., and $D_3 = 7.76$ in. Each cluster has the same directional characteristics for a given wavenumber-length product kD_n, where k is the wavenumber and D_n is the diagonal distance between the elements of the c_n cluster.

A key feature of the array processing is that the spatial resolution, defined here as the sensing area or width of the major directional lobe, is controlled independently of steering angle and frequency over a frequency range determined by the chosen spatial resolution. The methodology used is adapted from Brooks, et al. [14] and Marcolini and Brooks [21]. Figure 7 shows a theoretical contour plot over the wing-flap model of the spatial noise rejection or spatial admittance in dB level when cluster c_3 is steered to the intersection of the airfoil main element and the flap. The sensing area is defined here as that region within the 3 dB down contour. The rejection of (extraneous) noise regions over the side plates and nozzle opening is also shown. The result is for a frequency of 10 kHz, where $kD_3 = 36.38$. This contour result would be identical to that of $kD_2 = 36.38$ for 20 kHz and $kD_1 = 36.38$ for 40 kHz. Also shown are the results for 17.5 and 35 kHz, which are seen to have the same sensing area resolution. These results are determined from "blending" the clusters through the use of the sensor weighting W_m of Equation 1. The weighting function depends on cluster grouping and is calculated based on the desired resolution (defined by kD_0) compared to that existing for the particular frequency. For microphones m in group c_1, $W_m = W_{c1}$; in group c_2, $W_m = W_{c2}$; and in group c_3, $W_m = W_{c3}$, where

$$\left.\begin{aligned} W_{c1} &= \sigma_1^{.875} \\ W_{c2} &= 1 - \sigma_1^{.875} \\ W_{c3} &= 0. \end{aligned}\right\} 0 < \sigma_1 \leq 1$$

$$\left.\begin{aligned} W_{c1} &= 0 \\ W_{c2} &= \sigma_2^{.875} \\ W_{c3} &= 1 - \sigma_2^{.875} \end{aligned}\right\} 0 < \sigma_2 \leq 1 \qquad (1)$$

and the blending coefficients are defined

$$\sigma_1 = \frac{kD_2 - (kD)_0}{kD_2 - kD_1}$$
$$\sigma_2 = \frac{kD_3 - (kD)_0}{kD_3 - KD_2} \qquad (2)$$

The exponent of the coefficient, .875, for the SADA was found to differ slightly from the array of Brooks, et al. [14] and Marcolini and Brooks [21].

Unsteady Surface Pressure Sensors

The purpose of the unsteady surface pressure measurements is twofold: (1) quantify the wavenumber spectra over the surface, and (2) correlate surface pressure measurements with the far field acoustic measurements. The model is instrumented with 184 transducers for detailed unsteady surface pressure measurements; 96 of these transducers are located on the main element; 88 are located on the flap. The transducers on the flap-side edge are Endevco model 8507C; the transducers on the flap upper and lower surfaces are Kulite model LQ-34-064-5A. Because the data acquisition system can acquire data on only 32 transducers simultaneously, the transducers are grouped into 11 groups of 32. (Most of the transducers are located in several groups.) The groupings are shown in Figures 8 and 9, and are designed to facilitate the investigation of flow dynamics of the flap edge, cove, and the interaction between the main element and flap. The purpose of the individual groupings is summarized in Table 2. Because this paper focuses on the flap edge flow field, results presented here are limited to Group V.

Table 2. Instrumentation on Model used in Airframe Noise Testing.

Groups	Purpose
I, V	Flap edge flow
II, III	Main element - flap interaction
VI, IX	Main element - flap interaction
	Main element - flap interaction
	Main element trailing edge flow
	Cove flow
	Flap leading edge flow
VII,XII,X	Flap flow
XI	Main element trailing edge flow

Data Acquisition and On-Line Processing

The data acquisition system consists of two NEFF 495 transient data recorders which are controlled by a DEC AXP3400 workstation. Both NEFFs are controlled by the same external clock (set to 142.857 ksamples/second unless otherwise noted) and are operated in a block acquisition mode so that both acoustic and unsteady surface pressure data can be acquired simultaneously, and the resulting measurements correlated. The NEFF used for microphone array data acquisition consists of 36 14-bit acquisition channels. The NEFF used for the unsteady surface pressure sensors consists of 32 12-bit acquisition channels. Each channel has a maximum data

buffer size of 4 MBytes, allowing two million 2-byte samples to be taken per acquisition.

The signals from the unsteady surface pressure transducers pass through Precision amplifiers which provide up to 40 dB gain and AC-coupling. The power supplies for the amplifiers are 12-volt automobile batteries which are used to reduce electronic noise. Sixth-order Bessel anti-aliasing filters are set for a cut-off frequency of 50 kHz. A high pass filter is set at 300 Hz. The host DEC Alpha computer uses a NASA-developed software program which controls data acquisition system set up, data collections, quick look analysis, and archiving from menu driven graphics screens. The on-line data processing is done on a DEC alpha running the OSF/1 operating system. The system computes spectra and correlations, converts the information to engineering units, and saves the raw data for post-processing.

Post-Processing Data for Acoustic Arrays

The basic processing procedure for the array data consisted of three individual steps: the construction of cross-spectral matrices for the ensemble raw data set, the calculation of time delay corrections to account for shear layer refraction effects, and the beamformer calculations to generate one or more noise image maps at specified frequencies (LADA) or spectra/directivity plots (SADA). Each step of the processing is described below.

Cross spectral matrices

The first step in the post processing of each data set of data is the generation of the cross spectral matrix. The formation of the individual matrix elements is performed in terms of Fourier transformations of the original data ensemble. This is accomplished by converting the raw data obtained from the NEFF acquisition systems to engineering units by dividing the NEFF counts by 32768 and multiplying by the full scale range (in volts) and the transducer sensitivity (Pascals/volt).

The time pressure data for each acquisition is then segmented into a series of non-overlapping blocks each containing 2^{13} time samples. These blocks are Fourier transformed using a Hamming window to generate an ensemble of frequency domain data blocks. The individual cross spectral matrix entries of the upper triangular elements of the matrix are formed by computing the corresponding block-averaged cross spectra from the frequency data using the expression:

$$R_{ij}(f) = \frac{1}{NW_{ss}} \sum_{k=1}^{N} [X_{ik}^{*}(f) X_{jk}(f)] \qquad (3)$$

where W_{ss} is the data window weighting function, N is the number of points in the FFT, and X_{ik} and X_{jk} represent the frequency domain data block for the $k-th$ block of channels i and j, respectively. When $i = j$, the above expression reduces to the definition of the autospectra. The lower triangular elements of the matrix are obtained by complex conjugations of the Hermitian cross-spectral matrix.

Shear layer corrections

Testing in an open-jet facility requires that the effect of the shear layer on the propagation of the noise be accounted for. Corrections for these effects, based on the theory of Schlinker and Amiet [22] and Amiet [23], is included in the processing. To implement shear layer corrections for this experiment where the shear layer is highly curved, five hole pitot probe measurements were taken to map out the shear layer position. The experimental data is then fitted with a three dimensional surface used to define a continuous shear layer. Iteration is used to determine the intersection of acoustic ray paths from the array scanning plane points to the array microphones. The shear layer correction algorithm includes both amplitude and phase corrections. For the results presented in this paper only the phase corrections are applied.

Beamformer computations

Conventional frequency-domain beamforming is employed to extract the two-dimensional noise field maps from data obtained with the array [20]. The beamformer electronically "steers" the array to a predefined series of locations in space. For each steering location, a phase steering vector containing one entry for each microphone in the array is computed:

$$e = \begin{bmatrix} \exp\{-j[(\vec{k} \cdot \vec{x}_0) + \omega \Delta t_{0,shear}]\} \\ \vdots \\ \exp\{-j[(\vec{k} \cdot \vec{x}_{M-1}) + \omega \Delta t_{M-1,shear}]\} \end{bmatrix} \qquad (4)$$

where k is the local wavenumber , x is the distance from the survey location to each array microphone, M is the number of microphones and $\omega \Delta t_{m,shear}$ is the shear layer phase correction for microphone m. Using the steering vector and the cross spectral matrix computed previously, the shaded steered response power for the array at the current survey location is obtained from $P(e) = e^{T} W \hat{R} W^{T} e$ where W is the cluster weighting function for the array. Note for the LADA, the cluster weighting functions W_m are 1; for SADA the weighting functions are defined by Eqn. 1.

The noise source localization maps are represented as a series of contour plots with the levels propor-

tional to the steered response sound pressure level for the frequency under examination. Both narrowband and one-third octave bands can be processed with the beamformer system. The output of the array is represented as a summing of all the short-time spectra with each shifted an appropriate amount given the propagation time of the sound from the steering location to the sensor. This operation is represented mathematically by [20]:

$$Z(t,\omega) = \sum_{m=0}^{M-1} \frac{W_m}{r_m} Y_m(t,\omega) e^{j\omega t} e^{-j\omega \Delta_m} \qquad (5)$$

where W_m is the sensor weighting, r_m is the distance from the steering location to the m-th sensor, Y_m is the short-time Fourier transform for the m-th sensor, and Δ_m is the linear phase shift introduced to the m-th spectra.

Measurements

Base Aerodynamic Measurements

High-lift nature of flow established

In a properly designed main element-flap system, the elements interact [24]. The elements are close enough that the flow acceleration around the flap leading edge significantly reduces the required pressure recovery by the main element, but the elements are separate enough that the viscous boundary layers do not merge. In order to confirm that the nature of the flap flow resembles that of a high-lift system, detailed static pressure measurements were taken. Figure 10 shows the static pressure as a function of streamwise coordinate, x, normalized by the main element chord, c for locations at the mid-span of the flapped ($z/b = 0.75$) and unflapped ($z/b = 0.25$) sides of the airfoil for an angle-of-attack of 16 deg and a flap deflection angle of 29 deg in a freestream Mach number of 0.17. (Note that an angle-of-attack of 16 deg in an open jet facility is roughly equivalent to an angle-of-attack of 5 deg in a closed wall facility.) The flap flow field is dictated almost entirely by the flap deflection angle. The boundary layer is tripped on both the pressure side of the main element with a 1 in wide strip of serrated tape, and the leading edge of the flap at the flow stagnation point with a 0.25 in strip of serrated tape. The acceleration of the flow field at the trailing edge of the main element on the flapped side of the airfoil ($z/b = 0.75$), indicated by the increase in $-C_p$ (dotted line) at the trailing edge of the main element, suggests that there is sufficient flow through the gap between the main element and flap to increase lift on the main element. Pitot probe measurements were also taken to confirm that the viscous boundary layers do not merge. Comparison of the $-C_p$ distributions along the flapped and unflapped sides of the airfoil confirm that lift on the main element is increased by the presence of the flap. For the 29 deg flap deflection, the gap between the main element and flap is 0.402 in; the overlap is 0.108 in. Figure 11 illustrates the definition of gap and overlap used here. Similar conclusions about the high-lift nature of the configuration are drawn when the flap deflection angle is 39 deg, the gap is 0.402 in, and the overlap is .381 in. Thus, these are the flow conditions used in the acoustics experiments.

Flap edge flow physics

Flow measurements including oil flow and smoke visualization, pressure sensitive paint, and five hole probe measurements have been conducted at NASA Langley Research Center to investigate the flap edge flow physics. Discussion below focuses on five hole probe data taken by Radeztsky (unpublished) which illustrates the flap edge flow physics for the main element-flap configuration under the flow conditions tested.

• $M = 0.17$, $\alpha = 16\,\text{deg}$, $\delta_f = 29\,\text{deg}$

Figure 12 shows contour plots of dimensionless vorticity at several chordwise stations about the flap edge for a condition where the freestream Mach number is 0.17, the angle of attack is 16 deg, and the flap deflection angle is 29 deg. To obtain this figure, the velocity coordinate directions are rotated from the probe axis to the scanning plane. The velocity is normalized by the freestream velocity at the nozzle; the length is normalized by the flap chord. The coordinate x' in the figure is distance downstream of the flap leading edge, normalized by the flap chord. From this figure, it is clear that a dual vortex system is established near the flap leading edge. The presence of this dual vortex system under similar test conditions was also noted by Storms, et al. [8]. The primary vortex is formed near the bottom edge and grows in size in the streamwise direction until it fills the entire side edge. The weaker vortex on the suction surface grows moderately at the location near the flap mid-chord, the primary vortex extends beyond the flap-side edge, merges with the top vortex, and forms a single strong vortex. Computational studies [9] reveal that the separated shear layer at the bottom edge is a source of vorticity which wraps around the vortex and feeds it, resulting in a stronger vortex. The axial velocity in the core can attain speeds up to two times the freestream speed.

•$M = 0.17,\ \alpha = 16\,\text{deg},\ \delta_f = 39\,\text{deg}$

Figure 13 shows contours of vorticity at several chordwise stations in the vicinity of the flap edge for a freestream Mach number of 0.17, a 16 deg angle-of-attack, and a 39 deg flap deflection angle. This figure shows that the flow physics can change dramatically with flap deflection angle. Although the flow fields for both flap deflection angles sustain a dual vortex system, the details of the flow structure are seen to be very different. The vortices are stronger and the side edge vortex spills over to the upper flap surface sooner for the 39 deg flap deflection angle. Most interestingly, the vortex bursts in the 39 deg flap deflection case. The blank regions in the contour plots indicate regions in which the values measured by the five-hole probe were out of the probe's calibration range. This occurs when the local flow angularity is too high or the axial component of velocity is too low. The figure shows that at $x' = .59$ and $x' = .84$ there are significant regions of low axial velocity on the flap edge and within the vortex, typical of "bubble-type" or "axisymmetric" vortex bursting [25]. Reynolds averaged Navier-Stokes calculations confirm the bursting phenomenon at the high flap deflection angle, and will be the subject of a subsequent paper.

Initial LADA Measurements

Acoustic field maps produced by scanning the LADA over a plane parallel to the main element on the model pressure surface, and processing the acquired data with 4096 point FFTs, are presented in this section. The sampling rate for the data acquisition was 250 kHz. This data is preliminary in that the background noise levels have not been subtracted, and these tests were conducted before the installation of noise control features such as rounded side plate edges were complete. The effect of background noise is expected to be negligible for the results shown here. The effect of the noise control features will be determined when the LADA measurements are repeated with these features in place.

•$M = 0.17,\ \alpha = 16\,\text{deg},\ \delta_f = 29\,\text{deg}$

Typical acoustic field maps taken on the pressure side of the model at 16 deg angle-of-attack and 39 deg flap deflection angle and overlap of .381 in in a Mach 0.17 freestream flow are shown in Figure 14. The flow is from bottom to top and an outline of the wing and flap provides a reference for the noise sources that appear. In order to highlight the region about the flap edge, source localization maps are shown in the vicinity of the flap edge only. The origin of the plots is located at the juncture between the main wing trailing edge and the flap edge. In order to highlight the region about the flap edge, source localization maps are shown for the region in the vicinity of the flap edge only. Figure 14 shows the source localization map for 5 and 12.5 kHz. These single frequency results have a bandwidth of 61 Hz. Note that the location and strength of the locally dominant noise source is dependent on frequency. The source level diminishes with increasing frequency, and the map for 12.5 kHz shows array lobe patterns, indicating that the array is operating under low signal to noise conditions.

•$M = 0.17,\ \alpha = 16\,\text{deg},\ \delta_f = 39\,\text{deg}$

Typical acoustic field maps taken on the pressure side of the model at 16 deg angle-of-attack and 39 deg flap deflection angle in a Mach 0.17 freestream flow are shown in Figure 15. In order to highlight the region about the flap edge, source localization maps are shown for the region in the vicinity of the flap edge only. Because the source levels are higher for the 39 flap deflection angle case, figure 15 shows the source localization map for 20 kHz as well as for 5, 8 and 12.5 kHz. Note that the location and strength of the locally dominant noise source is dependent on frequency. The source level diminishes with increasing frequency, and the map for 12.5 and 20 kHz show array lobe patterns, indicating that the array is operating under low signal to noise conditions.

The results presented in Figures 14 and 15 show that the locally dominant source centroid changes with frequency. To further illustrate this trend, the position of the locally dominant noise source location, defined by the centroid of the source on the source localization maps for the test conditions above, is shown in Figure 16. This figure shows that along the flap-side edge, a trend exists for low frequency sound sources to be located near the flap trailing edge and high frequency sound sources to be located near the flap mid chord ($\delta_f = 29\,\text{deg}$) or the flap-main element juncture ($\delta_f = 39\,\text{deg}$). This trend of decreasing frequency with increasing streamwise distance is consistent with the increase in the scale of dominant flow structures, such as the side edge vortex, with increasing streamwise distance as illustrated in Figures 12 and 13. Kendall and Ahtye [4] also noted that lower frequencies were dominant near the flap trailing edge, and surmised that the growth of the flap-side edge vortex could be responsible for this trend.

Initial SADA Measurements

Prior to mounting the SADA on the test apparatus boom, the array and its processing software were calibrated with the use of a small speaker and a point source of sound placed at different locations in an

anechoic environment. The point source is the open end of a one-half inch diameter tube connected to a high-intensity, high-frequency acoustic driver. The microphones within the array were found to have negligible mutual interference; and reflections from the acoustically treated array frame were also negligible. The calibrations verified that SADA functioned completely as planned. For a broad range of frequencies, the theoretical and measured spatial distribution of noise rejection was found to be accurately matched. Another calibration procedure was performed as an integral part of the wing-flap model test. For this in-situ calibration, the point source is positioned at the junction of the flap edge and main element trailing edge. At each SADA measurement position and flow velocity, noise source mapping is used to validate the orientation and the accuracy of steering (which incorporates shear layer refraction calculations).

The measurement configuration is shown in Figure 4. For the SADA measurements reported here, refinements were completed to the model sideplate, nozzle lips, the downstream flow collector, and facility to minimize extraneous noise and reflections. SADA measurements were made for a model angle at $\alpha = 16$ deg and two flap angles, $\delta_f = 29$ deg and $\delta_f = 39$ deg, for various flow velocities and directivity positions. SADA measurement positions are sketched in Figures 17 and 18. The position of SADA in the Figure 4 photo corresponds to $\phi = -124$ deg in the sketch of Figure 18. The top view of the test setup is sketched in Figure 17 showing the azimuthal angle, ψ, measurement positions. For this paper, results will be shown for the pressure side of the model only along the model half span position, $\psi = 0$ deg, but at various elevation angles ϕ.

Figure 19 shows noise spectra measured for the model at $\alpha = 16$ deg and $\delta_f = 29$ deg, flow velocity at M = 0.17, and the SADA at $\psi = 0$ deg and $\phi = 107$ deg. This position corresponds to the perspective view of the test apparatus as seen in Figure 7, where spatial noise rejection for several frequencies is shown as dB contours over the surfaces. The spectrum with the highest levels is that of a single microphone in the SADA (as expected, all microphones were found to have essentially the same auto-spectra). Also shown is the spectrum of SADA when it is electronically steered to the flap edge region, as illustrated in Figure 7. The difference in levels of the two spectra represents the removal of unwanted noise from other regions of the test apparatus. For the SADA processing of $kD_0 = 36.38$, the width of the effective sensing area is about 10 inches for frequencies between 10 and 40 kHz. Outside this range, at 5 and 50 kHz for example, it is about 20 and 8 inches, respectively. So, at the lowest frequencies, the spectrum represents the noise from larger regions of the wing/flap model. But, at the higher frequencies shown the sensing area is little changed. Also shown in Figure 19 is the wind-off or background condition for the array. In the following data, such background spectra is subtracted appropriately from respective wind-on test case spectra.

For this same model flap angle ($\delta_f = 29$ deg) and SADA position ($\phi = 107$ deg), Figure 20 shows the effect of tunnel flow velocity on the noise radiated from the flap edge region. These SADA spectra have the background noise subtracted and questionable signal-to-noise spectral regions have been removed. These results show the general character of a Strouhal dependent broadband spectra expected from flow-surface interaction noise problems. However, the appearance of multiple broadband tonals at high frequencies for the higher flow speeds indicate aeroacoustic phenomena following different scaling characteristics than the lower frequency spectra. Although these are at very high frequency on this scale model, full scale aircraft would see such noise contributions in the important mid-frequency ranges of importance in annoyance criteria. In fact, most of the spectra shown would contribute significantly to this range.

It is important to point out that some features of the spectra shown appear to be related to test configuration and not to wing-flap aeroacoustics phenomena. The multi-peaked behavior at about 3 kHz and below is consistent with a sideplate reflection cancellation (at the drop-offs) and re-enforcement (at the peaks) effect. As previously mentioned, at low frequencies the width of the array sensing area approaches the model span, so reflections can add to the array's output. Therefore care should be taken in interpreting the results at low frequencies.

Figure 21 shows the spectra from the SADA for different elevation positions. With the exception of the most downstream position ($\phi = 56$ deg), the spectra are all within a few dB of one another over a broad portion of the frequency range. The results appear to show that, for the flap at $\delta_f = 29$ deg, the directivity is substantially uniform over a broad ϕ range with a drop-off in level downstream, consistent with that of a classical baffled dipole directivity.

Figure 22 show noise spectra dependence on tunnel flow velocity for the model flap at $\delta_f = 39$ deg. The presentation is the same as that of Figure 20, except for the flap angle change. Comparing Figure 22 with Figure 20, it is seen that with the exception of the very lowest frequencies all spectra have

uniformly increased, typically 10 dB, for the larger flap deflection. This level increase includes the high frequency tonals. Additional broadband noise for the higher flap deflection seems to have a distinct Strouhal dependence which is centered at about 3 to 5 kHz for M=0.17. It is apparent that an altered flow condition at the flap edge now dominates the radiated noise field. The directivity results are shown in Figure 23. It is seen that the directivity for $\delta_f = 39$ deg is much less uniform in the streamwise direction, compared to the relatively flat directivity for $\delta_f = 29$ deg. This is especially true for the non-uniform directivity for the spectral hump over the 3 to 5 kHz range and over the high frequency tonals.

The Strouhal dependence for the two flap angles is examined in Figure 24, where we have chosen to normalize one-third octave dB levels by an assumed Mach number to the fifth power dependence versus the Strouhal number based simply on the tunnel velocity and the flap chord dimension. The increased levels and increase in Strouhal number with the larger flap angle is clearly evident. A fifth power law dependence approximately fits the data for the small flap deflection at low frequencies, and at higher frequencies the power law dependence is higher. At larger flap deflection angles the power law dependence in the low frequency range is about 5.5.

Initial Unsteady Surface Pressure Measurements

Prior to acquiring data from the unsteady surface pressure sensors, an in-situ calibration was performed on each of the transducers using a NASA designed calibration unit. The calibration device uses a diaphragm capable of producing high signals up to 50 kHz as the drive element. The sensor amplitudes and phases were calibrated using a B&K Model 4133 microphone as the reference device. The pressure sensors over most of the model (Kulite model LQ-34-064-5A) responded well up to about 20 kHz. The pressure sensors on the flap edge (Endevco Model 8507C) responded well up to 50 kHz.

Although all of the wing-flap transducer groupings are shown in this report to emphasize the extent of data which will be available at the conclusion of this experiment, only data obtained from Group V will be discussed here. These data presented are preliminary in the sense that the full data base has not been evaluated, and background noise levels have not yet been subtracted from the measurements. The data presented here were collected simultaneously with the data from the SADA located at $\phi = 107$ deg and $\psi = 0$ deg, so that correlations between the far field acoustics and unsteady surface pressures may be made.

$M = 0.17$, $\alpha = 16$ deg, $\delta_f = 29$ deg

Figure 25 shows coherence as a function of frequency at three locations along the flap upper surface. The location of the sensors is also shown schematically in the figure, with the position downstream of the flap leading edge normalized by flap chord shown. The results are shown only to 20 kHz because these particular transducers failed to respond well above that frequency. Figure 25 shows change in coherence as a function of distance downstream of the flap upper surface. The coherence between sensors 10 and 11 near the flap leading edge has multiple peaks at levels of about 0.2. The coherence between sensors 12 and 13 is seen to peak at a level of about 0.6 over a wide frequency range. The coherence further downstream (sensors 14 and 15) is high, but limited in frequency range. Recalling the results presented in Figure 12, it is interesting to note that the region on the flap upper surface which corresponds to the broad frequency range peak coherence levels is approximately where the side edge vortex 'fills' the side edge, and begins to spill to the flap upper surface.

Figure 26 shows coherence levels as a function of downstream distance along the flap-side edge up to 50 kHz. The sensors on the flap-side edge show a change in the coherence level with downstream distance similar to the trend observed on the flap upper surface. One difference, however, is the breadth of the frequency range over which this peaked, high coherence feature exists. A very interesting dual peaked high coherence feature is apparent in the high frequency range of the coherence plots for sensors 2 and 3 and sensors 3 and 4. The high frequency coherence peaks correspond with the peaks in the acoustic spectra as measured by SADA and illustrated in Figure 19. The cross spectra for sensors 3 and 4 is shown in Figure 27 which shows very significant amplitude levels up to about 10 kHz, and from about 40 to 50 kHz. The cross-spectral phase also shows very clear linear phase relationships between the measurements taken with sensors 3 and 4. The cross spectral phase in the 40-50 kHz range shows rapid phase changes, which suggests the existence of multiple sources.

$M = 0.17$, $\alpha = 16$ deg, $\delta_f = 39$ deg

Figure 28 shows coherence along the flap upper surface as a function of distance downstream of the flap leading edge. The trends are similar to those observed for the $\delta_f = 29$ deg case, but the coherence levels are higher closer to the flap leading edge (e.g.

coherence for sensors 10 and 11 peaks at 0.4 for δ_f = 39 as opposed to 0.2 for δ_f = 29 deg) and lower for the sensors closer to the trailing edge (max peak above 0.2 for δ_f = 39 deg, max peak of 0.7 for δ_f = 29 deg).

The coherence along the flap-side edge is shown in Figure 29. The results are similar to those presented for the δ_f = 29 deg case, but the dual-peaked coherence feature present between 40 and 50 kHz is lower than in the δ_f = 29 deg case. The cross-spectra for sensors 3 and 4 is shown in Figure 30. Comparison of Figures 27 and 30 shows that the cross spectral amplitude is significantly higher for δ_f = 39 in the frequency range from 4-8 kHz, and that the frequency of the cross spectral peaks in the 40-50 kHz range is higher. Both of these trends are consistent with differences in the far field spectra (Figures 19 and 22).

Summary

Aeroacoustic measurements are currently in progress in the NASA Langley Quiet Flow Facility to investigate the mechanisms of sound generation in high-lift wing configurations. This paper provides an overview of the testing of a wing with a half span flap under high-lift conditions, and focuses on results pertaining to the flap-side edge. The experiment utilizes three measurement systems developed for this study: two directional arrays used to localize and characterize the noise sources, and an array of unsteady surface pressure transducers used to characterize wave number spectra and correlate with acoustic measurements. Experiments are currently being conducted, but some initial results are presented here. Sound source localization maps obtained from the large aperture directional array show that locally dominant noise sources exist on the flap-side edge, and sound pressure level increases with flap deflection angle. The spectral distribution of the noise sources along the flap-side edge shows a decrease in frequency of the locally dominant noise source with increasing distance downstream of the flap leading edge. This trend of decreasing frequency with increasing streamwise distance is consistent with the increase in the size of dominant flow structures, such as the side edge vortex, with increasing streamwise distance. A small aperture directional array is used to quantify the spectra and directivity of the sound sources. Spectra are presented which show general spectral characteristics of Strouhal dependent flow-surface interaction noise. However, the appearance of multiple broadband tonal features at high frequency indicates the presence of aeroacoustic phenomenon following different scaling characteristics. An increase in flap deflection angle is shown to increase the sound pressure level over much of the measured frequency range. The scaling of the high frequency aeroacoustic phenomenon is found to be different for the two flap deflection angles tested. A fifth power law dependence approximately fits the low frequency data for the small flap deflection, and at higher frequencies the power law dependence is higher. At larger flap deflection, the power law dependence in the corresponding frequency range is about 5.5. Initial analysis of unsteady surface pressures in the vicinity of the flap edge show high coherence levels between adjacent sensors on the flap-side edge and on the flap edge upper surface in a region which appears to correspond closely to where the flap-side edge vortex begins to spill over to the flap upper surface. The frequency ranges where these high levels of coherence occur on the flap surface are consistent with the frequency ranges in which dominant features appear in far field acoustic spectra measured by the small aperture directional array.

Future work will include continuation of this experiment to localize sound sources and quantify their spectral and directivity characteristics under several operating conditions. Direct correlations between the unsteady surface pressures and far field sound are also planned for future analyses. Aeroacoustic testing of additional configurations, such as a slat-wing-flap configuration, will also be conducted. The aeroacoustic measurements will be analyzed in concert with detailed flow computations and aerodynamic measurements to develop a better understanding of the mechanisms of airframe noise.

Acknowledgments

The authors are pleased to acknowledge Dr. Ron Radeztsky of HTC for providing the data presented in the Base Aerodynamic Measurements section of this paper. The authors also gratefully acknowledge Dave DeVilbiss and Stuart Pope, both of Lockheed-Martin, for data processing support and computer code development, and Phil Grauberger of Wyle Laboratories for data acquisition system support and instrumentation trouble-shooting.

References

1. David G. Crighton. Airframe Noise. In Harvey H. Hubbard, editor, *Aeroacoustics of Flight Vehicles: Theory and Practice*, volume 1, pages 391-447. NASA RP 1258, 1991.

2. Patricia J. W. Block. Assessment of Airframe Noise. *Journal of Aircraft*, 16(12):834-841, Sept. 1979.

3. James M. Kendall. Measurments of Noise Produced by Flow Past Lifting Surfaces. AIAA 78-239, 1978.

4. J.M. Kendall and W.F. Ahtye. Noise Generation by a Lifting Wing/Flap Combination at Reynolds Numbers to $2.8x10^6$. AIAA 80-0035, 1980.

5. M. R. Fink and R.H. Schlinker. Airframe Noise Component Interaction Studies. AIAA 79-0668, 1979.

6. Wendall R. Miller, William C. Meecham, and Warren F. Ahtye. Large Scale Model Measurements of Airframe Noise Using Cross-Correlation Techniques. *Journal of the Acoustical Society of America*, 71(3):591–599, March 1982.

7. S. A. McInerny, W. C. Meecham, and P. T. Soderman. An Experimental Investigation of Wing Tip Turbulence with Applications to Aerosound. AIAA 86-1918, July 1986.

8. Bruce L. Storms, Timothy T. Takahashi, and James C. Ross. Aerodynamic Influence of a Finite-Span Flap on a Simple Wing. SAE Paper 951977, Sept. 1995.

9. Mehdi R. Khorrami, Bart A. Singer, and M.A. Takallu. Analysis of Flap Side-Edge Flowfield for Noise-Source Modeling. ASME 97NV22, 1997.

10. A. R. George, F. E. Najjar, and Y. N. Kim. Noise Due to Tip Vortex Formation on Lifting Rotors. AIAA 80-1010, June 1980.

11. A. R. George and Shan-Tak Chou. Broadband Rotor Noise Analysis. NASA CR 3797, April 1984.

12. T.F. Brooks and M.A. Marcolini. Airfoil Tip Vortex Formation Noise. AIAA 84-2308, 1984.

13. Thomas F. Brooks, D. Stuart Pope, and Michael A. Marcolini. Airfoil Self-Noise and Prediction. NASA Reference Publication 1218, 1989.

14. T.F. Brooks, M.A. Marcolini, and D.S. Pope. A Directional Array Approach for the Measurement of Rotor Noise Source Distributions with Controlled Spatial Resolution. *Journal of Sound and Vibration*, 112(1):192–197, 1987.

15. Jay C. Hardin. Noise Generation at the Side Edges of Flaps. AIAA 80-0978, 1980.

16. Rahul Sen. Local Dynamics nd Acoustics in Simple 2D Model of Airfoil La eral-Edge Noise . AIAA 96-1673, 1996.

17. Jay C. Hardin and J. Martin Flap Side-Edge Noise: Analysis of Sen's Mode AIAA 96-1674, 1996.

18. Harvey H. Hubbard and Jan es C. Manning. Aeroacoustic Research Faciliti s at NASA Langley Research Center. NASA M 84585, 1983.

19. James R. Underbrink. Practic l Considerations in Focused Array Design fo Passive Broad-Band Source Mapping Applic tions. Master's thesis, The Pennsylvania Stat University, May 1995.

20. Don H. Johnson and Dan E. Dudgeon. *Array Signal Processing*. Prentice H ll, 1993.

21. M.A. Marcolini and T.F. Bro ks. Rotor Noise Measurement Using a Directic nal Array. AIAA 87-2746, 1987.

22. R.H. Schlinker and R.K. An et. Shear Layer Refraction and Scattering of S ound. AIAA 80-973, 1980.

23. R. K. Amiet. Refraction of Sound by a Shear Layer. *Journal of Sou d and Vibration*, 58(3):467–482, Sept. 1978.

24. A.M.O. Smith. High-Lift Aer dynamics. *Journal of Aircraft*, 12(6), June 19 75.

25. Turgut Sarpkaya. On station ry and travelling vortex breakdowns. *Journal of Fluid Mechanics*, 45(3):545–559, 1971.

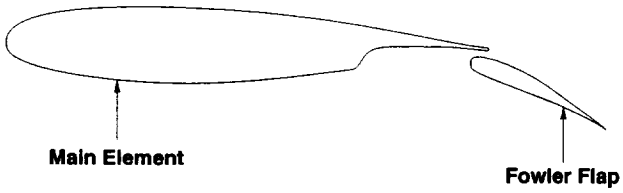

Figure 1. Cross section of model.

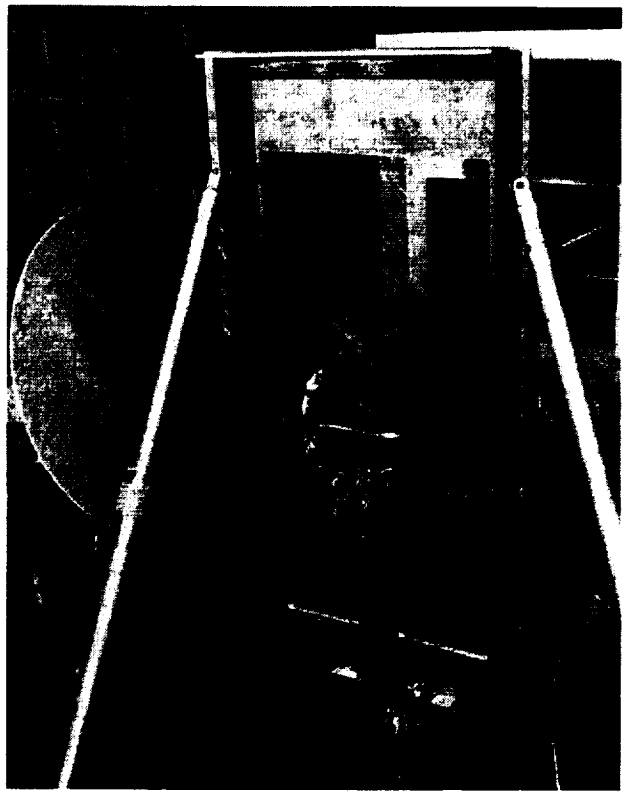

Figure 3. LADA installed in QFF.

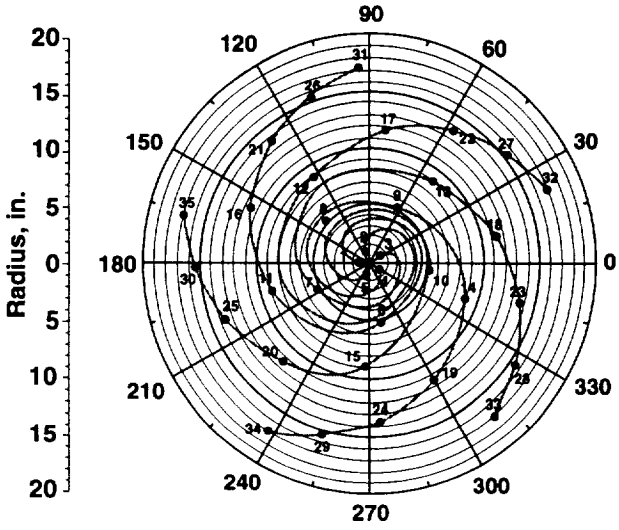

Figure 2. LADA microphone locations and pattern.

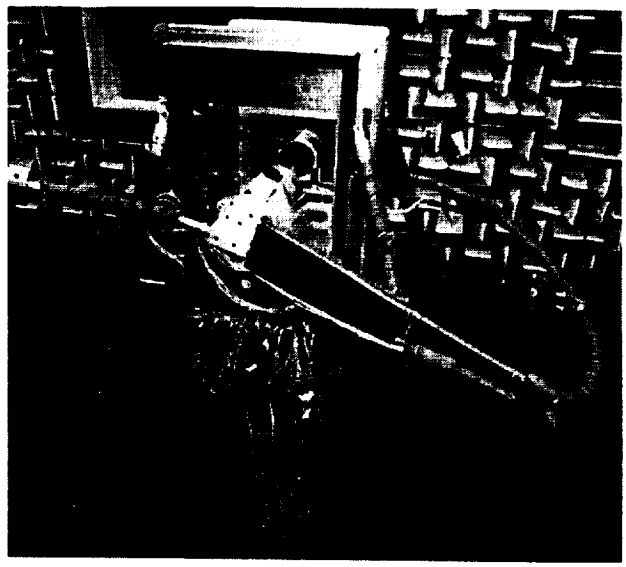

Figure 4. SADA mounted on pivotal boom in QFF.

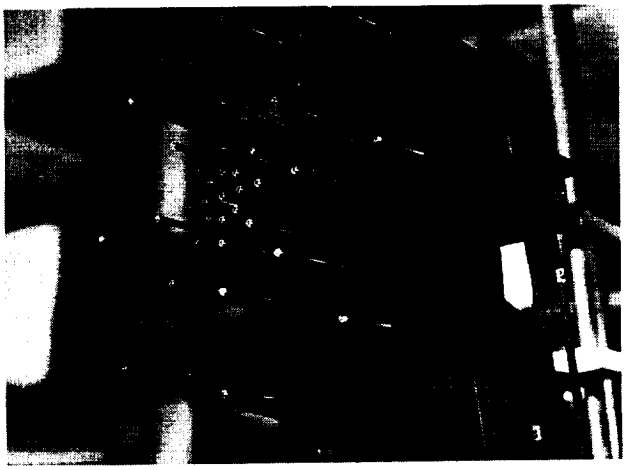

Figure 5. SADA.

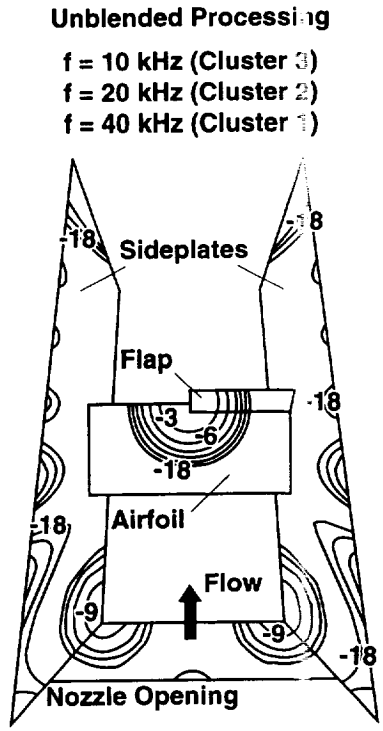

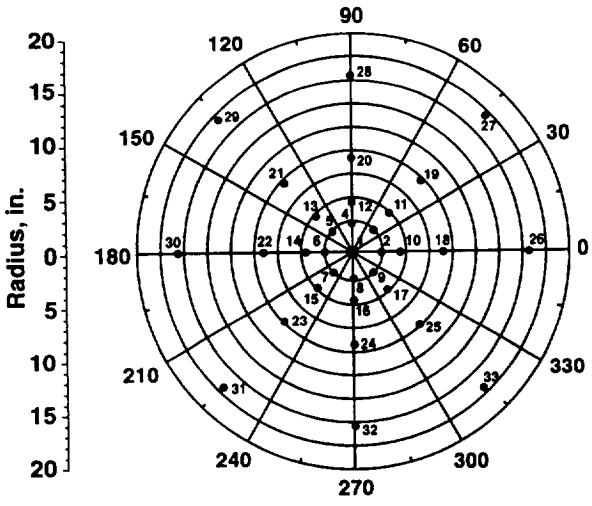

Figure 6. SADA microphone positions.

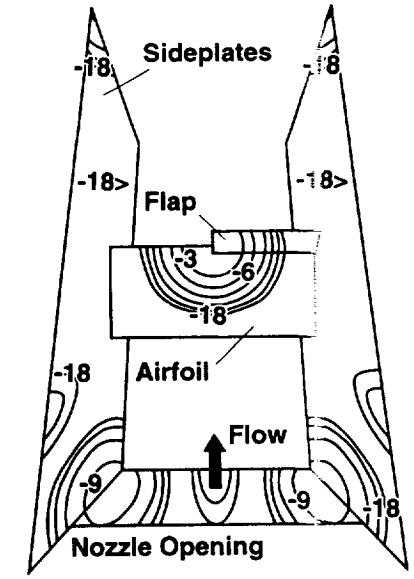

Figure 7. Theoretical spatial noise rejection of SADA on wing-flap model.

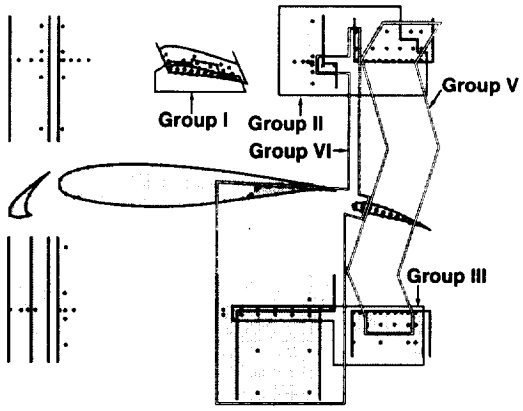

Figure 8. Unsteady surface pressure measurem locations and groupings. Side view taken at the h span station is shown in the center. Top and bottom views of the half span section are shown on the top and bottom of the figure, respectively. Group I is shown as an isometric view of the flap edge.

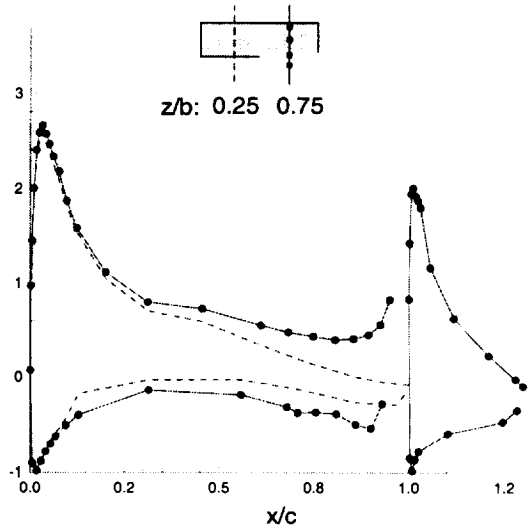

Figure 10. Pressure coefficient distribution along unflapped (z/b= 0.25) and flapped (z/b= 0.75) sections of the multi-element configuration tested. (Data courtesy of R. Radeztsky.)

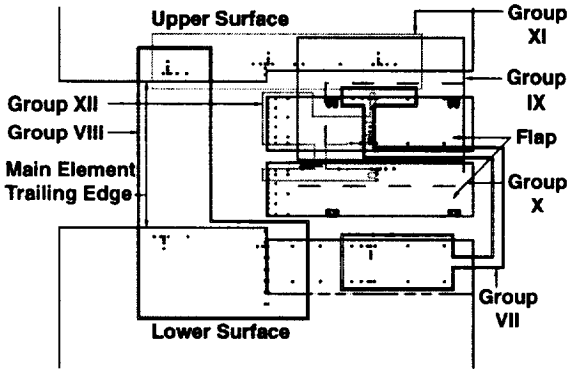

Figure 9. Unsteady surface pressure measurement locations and groupings. Top and bottom views of entire main element and flap surfaces.

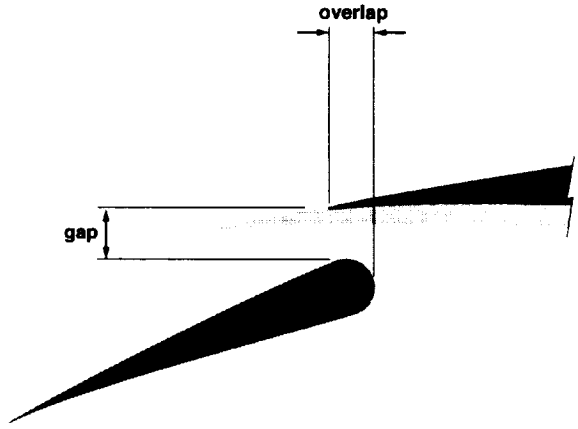

Figure 11. Definitions of the gap and overlap. Shaded region in background is the main element trailing edge of the unflapped side of the model.

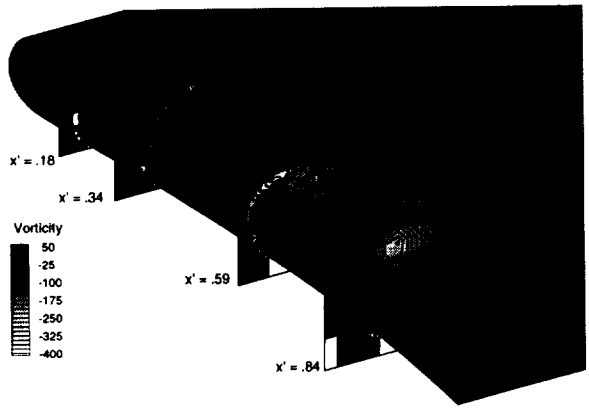

Figure 12. Measured contours of vorticity in vicinity of flap edge. $\alpha = 16\,\text{deg}, \delta_f = 29\,\text{deg}$. (Courtesy of R. Radeztsky.)

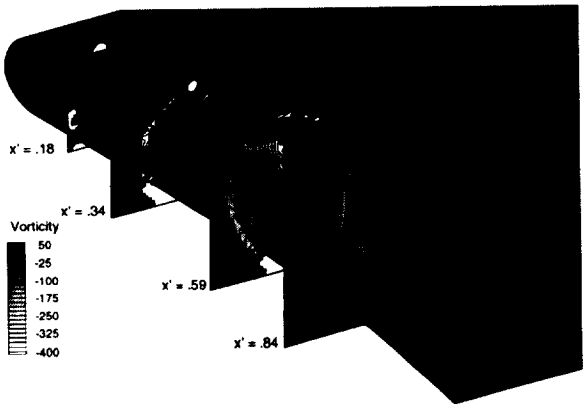

Figure 13. Measured contours of vorticity in vicinity of flap edge. $\alpha = 16\,\text{deg}, \delta_f = 39\,\text{deg}$. (Courtesy of R. Radeztsky.)

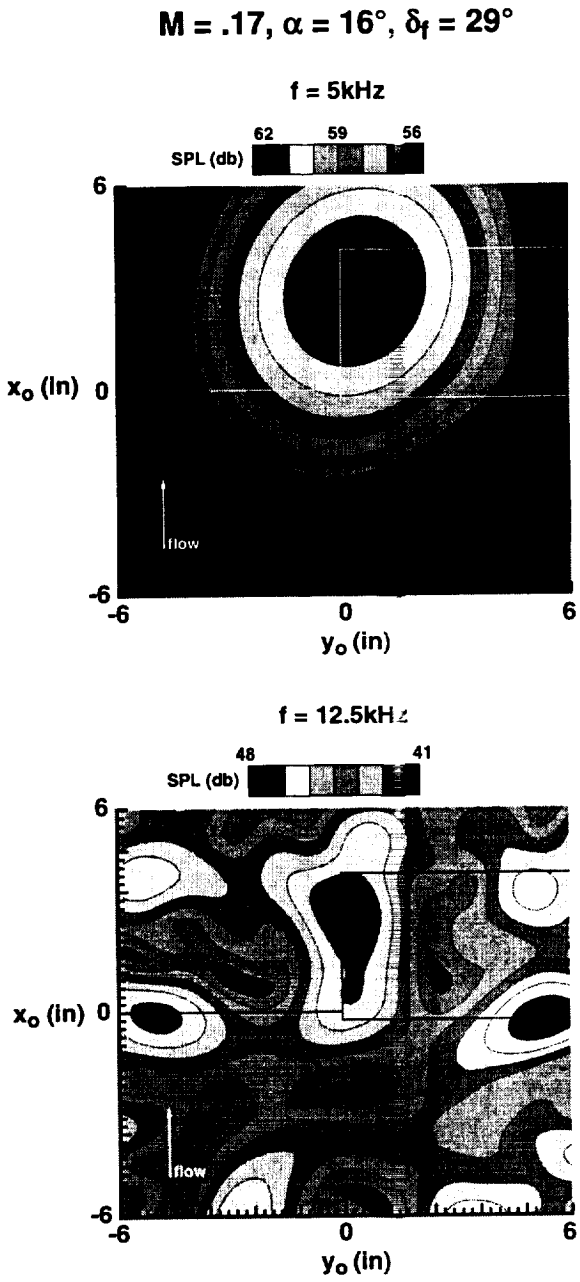

Figure 14. Sound source localization maps. $M = 0.17$, , $\alpha = 16\,\text{deg}$, $\delta_f = 29\,\text{deg}$

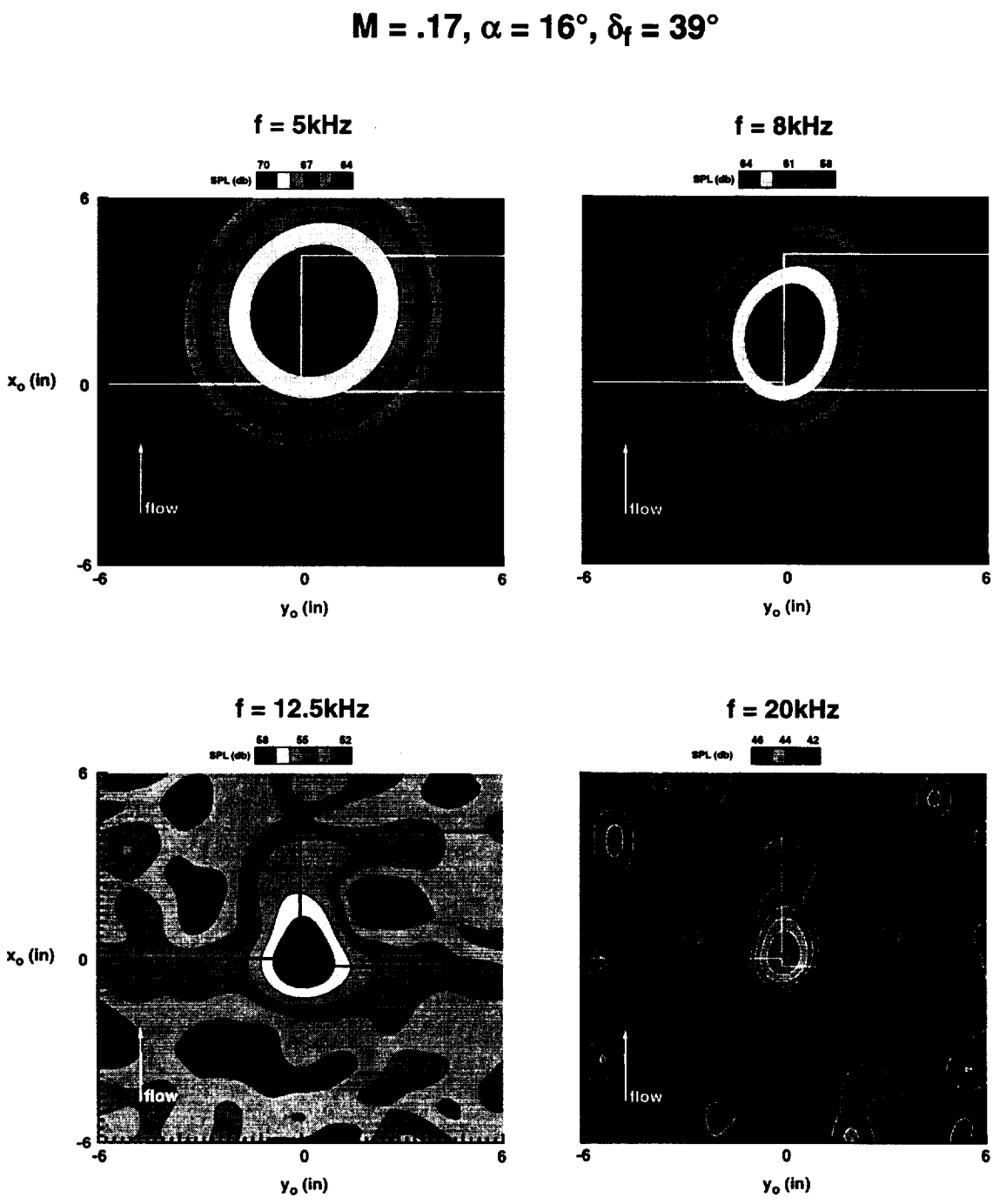

Figure 15. Sound source localization maps. $M = 0.17$, $\alpha = 16\,\text{deg}$, $\delta_f = 39\,\text{deg}$.

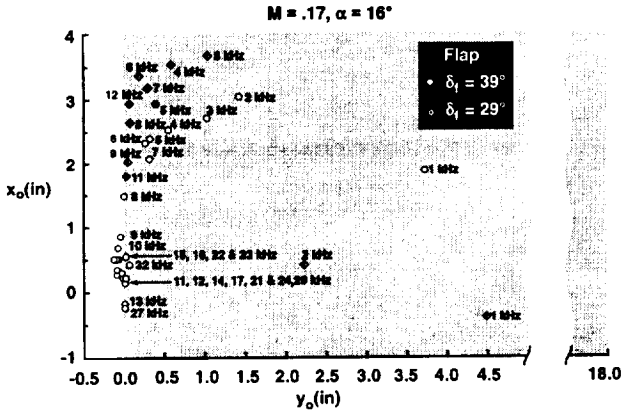

Figure 16. Locally dominant noise source centroid locations on the flap. Origin denotes flap and main element juncture. $M = 0.17$, $\alpha = 16$ deg.

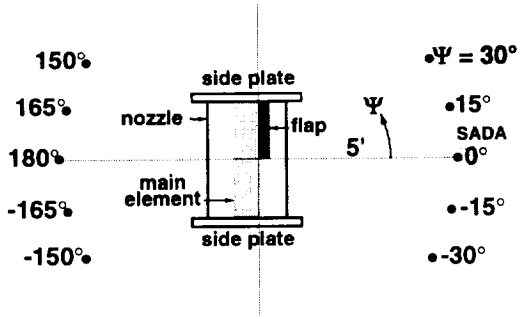

Figure 17. Positions for directivity measurements-top view.

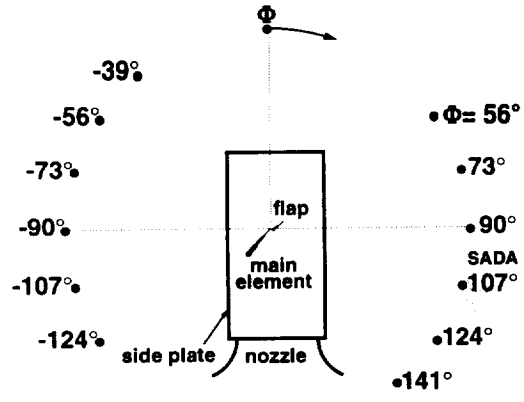

Figure 18. Positions for directivity measurements-Side view.

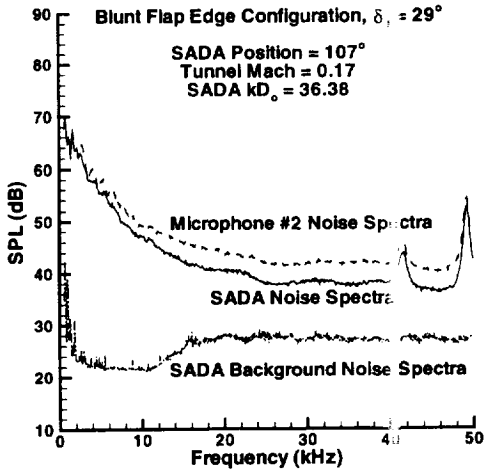

Figure 19. Spectra. $M = 0.17$, $\alpha = 16$ deg, $\delta_f = 29$ deg. Results shown for 87 Hz bandwidth.

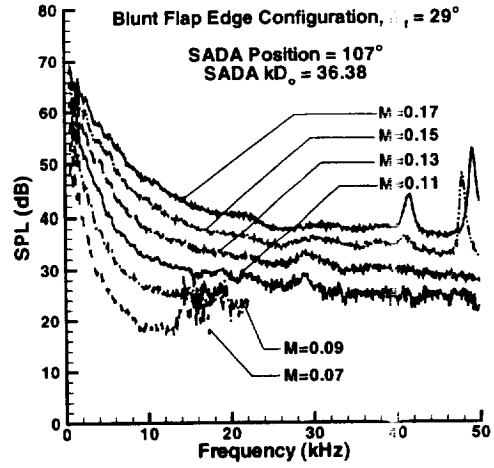

Figure 20. Effect of tunnel Mach number on radiated noise. Results shown for 87 Hz bandwidth.

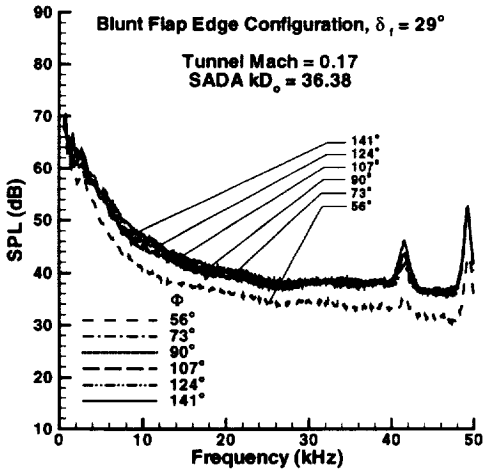

Figure 21. Directivity of noise on airfoil pressure side. Results shown for 87 Hz bandwidth.

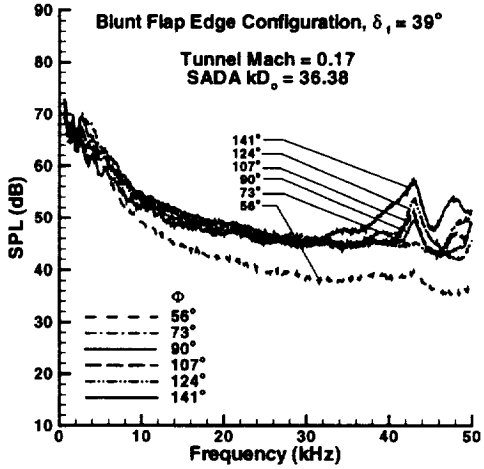

Figure 23. Directivity of spectra. $\alpha = 16\,\text{deg}$, $\delta_f = 39\,\text{deg}$. $M = 0.17$. Results shown for 87 Hz bandwidth.

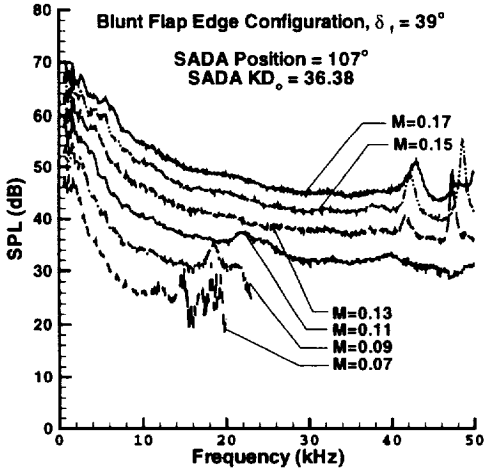

Figure 22. Effect of flow velocity on noise spectra. $\alpha = 16\,\text{deg}$, $\delta_f = 39\,\text{deg}$. Results shown for 87 Hz bandwidth.

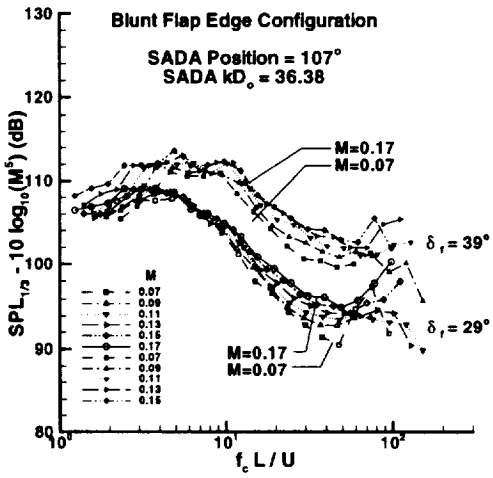

Figure 24. Strouhal dependence. $\alpha = 16\,\text{deg}$. Both flap angles shown. L is flap chord; U is tunnel velocity; f_c is one-third octave center frequency.

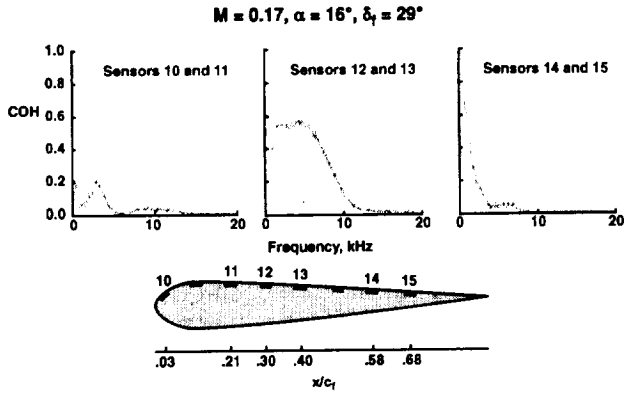

Figure 25. Coherence along flap upper surface. $M = 0.17$, $\alpha = 16\,\text{deg}$, $\delta_f = 29\,\text{deg}$. Results shown for 17.4 Hz bandwidth.

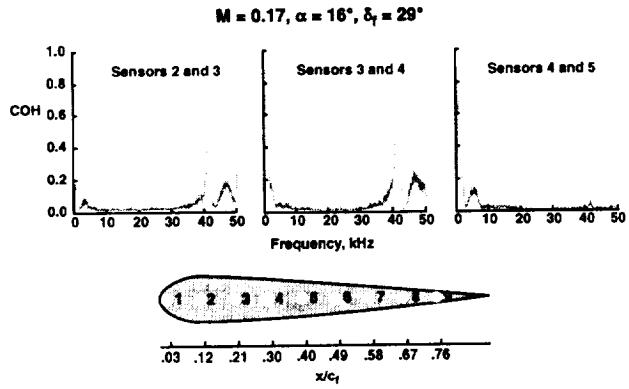

Figure 26. Coherence along flap-side edge. $M = 0.17$, $\alpha = 16\,\text{deg}$, $\delta_f = 29\,\text{deg}$. Results shown for 17.4 Hz bandwidth.

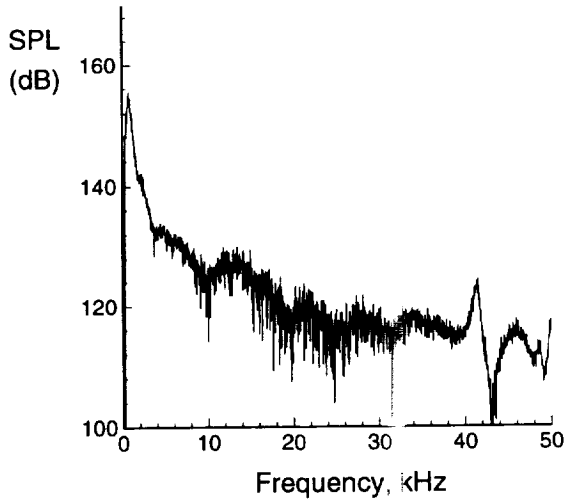

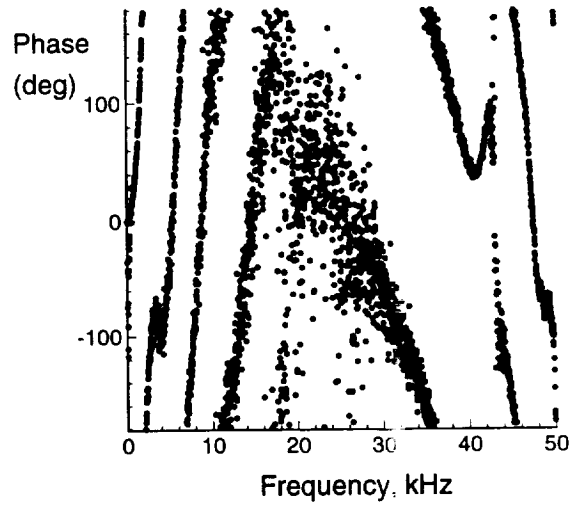

Figure 27. Cross spectra for sensors 3 and 4. $\delta_f = 29\,\text{deg}$. Results shown for 17.4 Hz bandwidth.

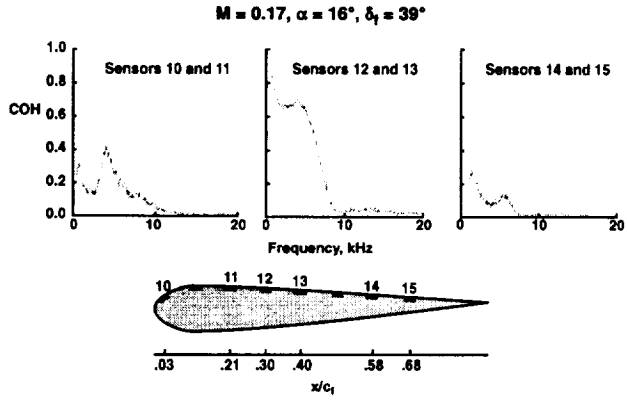

Figure 28. Coherence along flap upper surface. $M = 0.17$, $\alpha = 16\,\text{deg}$, $\delta_f = 39\,\text{deg}$. Results shown for 17.4 Hz bandwidth.

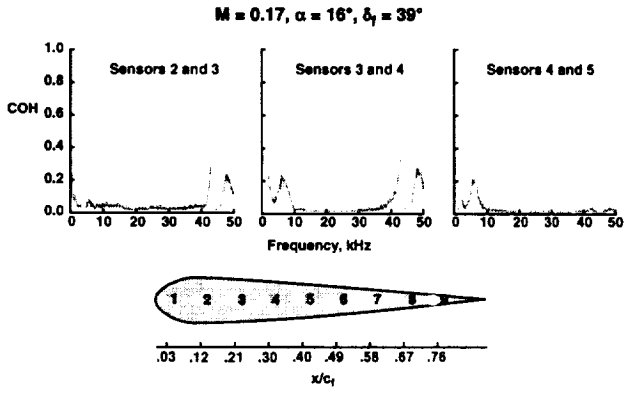

Figure 29. Coherence along flap-side edge. $M = 0.17$, $\alpha = 16\,\text{deg}$, $\delta_f = 39\,\text{deg}$. Results shown for 17.4 Hz bandwidth.

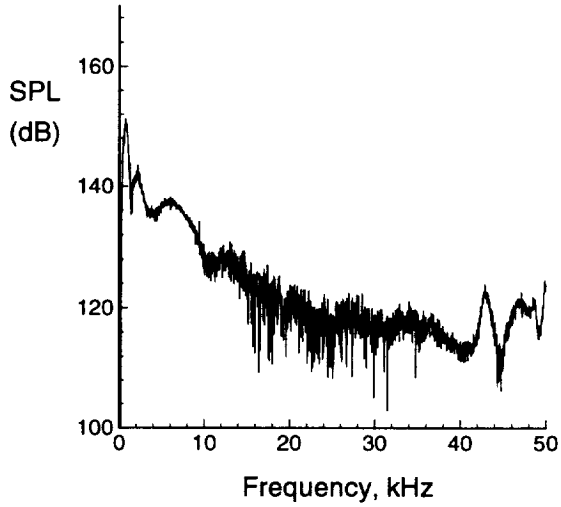

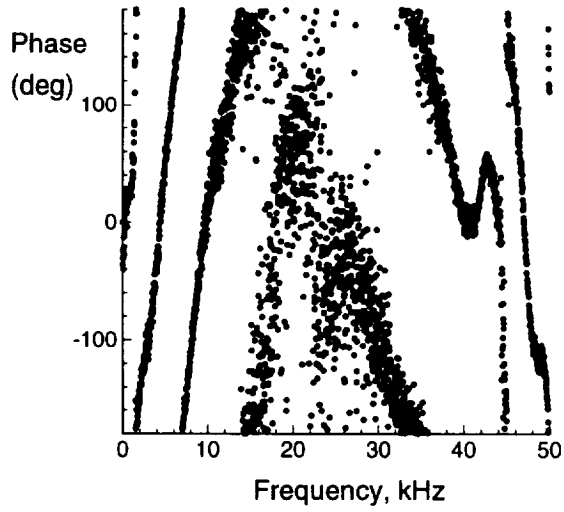

Figure 30. Cross spectra for sensors 3 and 4. $\delta_f = 39\,\text{deg}$. Results shown for 17.4 Hz bandwidth.